Activation of the Binuclear Metal Center through Formation of Phosphotriesterase−Inhibitor Complexes†

Cynthia R. Samples,‡ Frank M. Raushel,‡ and Victoria J. DeRose*,§

Department of Chemistry, P.O. Box 30012, Texas A&M University, College Station, Texas 77842-3012, and Department of Chemistry, 1253 University of Oregon, Eugene, Oregon 97403-1253

Received September 19, 2006; Revised Manuscript Received December 20, 2006

ABSTRACT: Phosphotriesterase (PTE) from *Pseudomonas diminuta* is a binuclear metalloenzyme that catalyzes the hydrolysis of organophosphate nerve agents at rates approaching the diffusion-controlled limit. The proposed catalytic mechanism postulates the interaction of the substrate with the metal center and subsequent nucleophilic attack by the bridging hydroxide. X-band EPR spectroscopy was utilized to monitor the active site of Mn/Mn-substituted PTE upon addition of two inhibitors, diisopropyl methyl phosphonate and triethyl phosphate, and the product of hydrolysis, diethyl phosphate. The effects of inhibitor and product binding on the magnetic properties of the metal center and the hydroxyl bridge were evaluated by measuring changes in the features of the EPR spectra. The EPR spectra support the proposal that the binding of substrate analogues to the binuclear metal center diminishes the population of hydroxide-bridged species. These results, in conjunction with previously published kinetic and crystallographic data, suggest that substrate binding via the phosphoryl oxygen at the β-metal weakens the coordination of the hydroxide bridge to the β-metal. The weakened coordination to the β-metal ion increases the nucleophilic character of the hydroxide and is coupled to the increase in the electrophilic character of the substrate.

Phosphotriesterase (PTE[1]) from *Pseudomonas diminuta* is a zinc metalloenzyme found in soil bacteria that catalyzes the hydrolysis of organophosphate triesters at rates approaching the diffusion-controlled limit (*1*). Interest in PTE for the catalytic degradation of organophosphate nerve agents and detoxification of agricultural pesticides requires a clearer understanding of the mechanism for the enzymatic hydrolysis of these compounds. While a natural substrate has not been identified, a broad variety of organophosphate esters are hydrolyzed by this enzyme. The hydrolysis reaction of the insecticide paraoxon that is catalyzed by PTE is shown in Scheme 1. Characterization of PTE by X-ray crystallography and EPR spectroscopy, and an analysis of the kinetic properties of this enzyme, have provided significant mechanistic insight into the structure of the active site and the limits to the catalytic prowess of this remarkable enzyme (*2*, *3*).

The active site of PTE contains a binuclear metal center that is embedded within a $(\beta/\alpha)_8$-barrel structural motif (*4*). Two unique metal sites are observed with the α-metal coordinated by two histidines and an aspartate, whereas the β-metal is coordinated by two other histidines and one or two water ligands depending on the identity of the metal ion (*5*). The two metals are bridged by a carboxylated lysine and a hydroxide from solvent. Both metals are required for full catalytic activity, and they bind cooperatively to the apoenzyme during the self-assembly of the binuclear metal center (*6*, *7*). Substitution of the native Zn ions at the active site with divalent Mn, Co, Ni, or Cd results in the retention of full catalytic activity (*6*).

Scheme 1

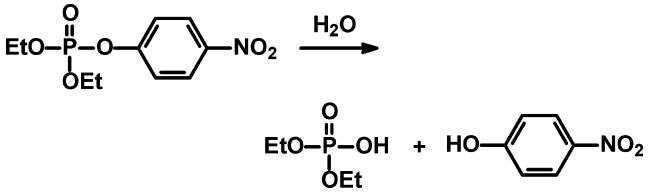

Prior experiments have unveiled significant details of the catalytic reaction mechanism. X-ray crystal structures of enzyme-bound substrate analogues have been used to support the proposal that binding of substrates in the active site occurs at the β-metal site through direct ligation of the phosphoryl oxygen (*3*, *8*). Polarization of the phosphoryl−oxygen bond of the substrate by the metal center is further supported by a comparison of the kinetic constants for the hydrolysis of phosphate and thiophosphate substrates with zinc- and cadmium-substituted variants of PTE (*9*). The nucleophile utilized for cleavage of the phosphotriester bond was identified as the hydroxide that bridges the two metals through correlated changes in the electron paramagnetic resonance (EPR) spectra and the kinetic constants as a function of pH (*6*, *11*). These findings highlight three major components of the reaction mechanism for PTE: (i) the metal center increases the electrophilicity of the phosphorus center

† This work was supported in part by the NIH (GM 68550 to F.M.R.), the NSF (CHE-0111696 to V.J.D. and CHE-0092010 for the Texas A&M EPR facilities), and the Robert A. Welch Foundation (A-1314 to V.J.D.).

* To whom correspondence may be addressed. Telephone: 541-346-3568. Fax: 541-346-0487. E-mail: derose@uoregon.edu.

‡ Texas A&M University.

§ University of Oregon.

[1] PTE, phosphotriesterase; EPR electron paramagnetic resonance; HEPES, *N*-2-hydroxyethylpiperazine-*N*′-2-ethanesulfonic acid; CHES, 2-(cyclohexylamino)ethanesulfonic acid; DIMP, diisopropyl methyl phosphonate; TEP, triethyl phosphate; DEP, diethyl phosphate.

10.1021/bi061951d CCC: $37.00
Published on Web 02/22/2007

Chart 1

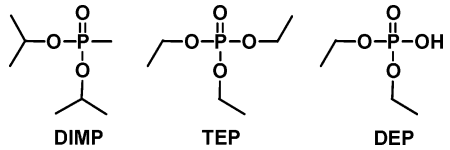

via polarization of the phosphoryl oxygen bond, (ii) the metal center provides the nucleophile for hydrolysis by lowering the pK_a of the coordinated water molecule, and (iii) the metal center binds the substrate to optimize the three-dimensional positioning of nucleophile and electrophile with respect to one another.

The influence of substrate binding on the metal center and the consequential effects on the hydroxide bridge have not been investigated. In the analogous active site of dihydroorotase (DHO), it has been proposed that a weakening of the bond between the hydroxide bridge and the β-metal occurs upon substrate binding based upon the asymmetrical metal−hydroxide distances in the crystal structure of DHO in the presence of dihydroorotate (*12*). A weakening of the hydroxide−metal bond to M_β in PTE would enhance the nucleophilic character of the hydroxide in proximity to the phosphorus center of the substrate. The hydroxide bridge is present in all of the X-ray crystal structures of Zn/Zn-PTE with an inhibitor bound to the active site (*3*, *8*).

In this paper, we investigate the effects of inhibitor and product binding on the properties of the metal center and the hydroxide bridge using EPR spectroscopy. EPR spectra of Mn/Mn-PTE are evaluated to establish the perturbations to the metal center upon addition of diisopropyl methyl phosphonate (DIMP), triethyl phosphate (TEP), and diethyl phosphate (DEP). The structures of these inhibitors are shown in Chart 1.

MATERIALS AND METHODS

Materials. DIMP, TEP, and all buffers were purchased from Sigma except for *N*-(2-hydroxyethyl)piperazine-*N*′-2-ethanesulfonic acid (HEPES), which was purchased from United States Biochemical. DEP was synthesized by Dr. Yingchun Li of Texas A&M University. Bacterial cell growth protocols, enzyme purification, preparation of apoenzyme, and reconstitution of PTE with manganese were performed as previously described (*6*).

Kinetic Measurements. The values of k_{cat} and k_{cat}/K_m for MnMn-PTE were determined by measuring the change in absorbance at 347 nm upon hydrolysis of paraoxon (20−2000 μM) to *p*-nitrophenol ($\epsilon_{347} = 5.1 \times 10^4$ M^{-1} cm^{-1}) and diethyl phosphate in 100 mM HEPES buffer at 30 °C with a $Spectra_{max}$ PLUS 384 plate reader from Molecular Devices. The inhibition constants for DIMP and DEP were determined by measuring the change in absorbance at 400 nm upon hydrolysis of paraoxon in the presence of each compound.

Data Analysis. The kinetic constants were obtained by fitting the data to eq 1, where v is the initial velocity, k_{cat} is

$$v/E_t = (k_{cat}A)/(K_m + A) \quad (1)$$

the turnover number, K_m is the Michaelis constant, and A is the substrate concentration. The competitive inhibition constants, K_i, for DIMP and DEP with Mn/Mn-PTE in the presence of paraoxon as the substrate were determined by fitting the data to eq 2, where I is the inhibitor concentration

$$v/E_t = k_{cat}A/(K_m(1 + I/K_i) + A) \quad (2)$$

and the other constants have been previously defined.

EPR Sample Preparation. Mn/Mn-substituted PTE samples of ∼1.0 mg/mL, pH 8.0, were concentrated to ∼20 mg/mL using a YM-10 Centricon microconcentrator from Amicon. All protein was loaded onto a PD-10 Sephadex G-25 desalting column from Amersham to remove unbound metal from the protein sample. All EPR samples were frozen in liquid nitrogen at concentrations of 100−200 μM PTE (3.6−7.3 mg/mL) containing ∼30% (v/v) glycerol in 50 mM HEPES at pH 8.0. EPR samples containing DIMP, TEP, or DEP were frozen after the samples sat on ice for 30 min. The protein concentrations were determined by measuring the absorbance at 280 nm using an extinction coefficient of 29 300 M^{-1} cm^{-1}.

EPR Spectroscopy. X-band EPR measurements were obtained using a Bruker ESP 300 spectrometer with a TE_{102} cavity, an Oxford Instruments liquid helium cryostat, an HP 5352B microwave frequency counter, and a Bruker ER 041XG microwave bridge. The magnetic field modulation frequency was 100 kHz, and the modulation amplitude was 15 G for samples containing DIMP and TEP and 20 G for all other samples. EPR spectra were obtained at 10 K, unless designated otherwise, under nonsaturating power conditions of 2 mW. Temperature-dependent studies were performed from 3.6 to 60 K for all samples.

RESULTS

Kinetic Constants. The values of k_{cat}, k_{cat}/K_m, and K_m for the hydrolysis of paraoxon by Mn/Mn PTE are 3400 s^{-1}, 1.1×10^7 M^{-1} s^{-1}, and 310 μM, respectively. The compounds DIMP and DEP were found to be competitive inhibitors of Mn/Mn-PTE with K_i values of 17 ± 1 and 30 ± 2 mM, respectively (data not shown).

EPR Spectra of Mn/Mn-PTE. The EPR spectrum of Mn/Mn-PTE is complex and consists of multiple sets of 11-line splittings separated by 45 G, indicative of spin-coupled binuclear (Mn(II)) systems (Figure 1A). These binuclear $(Mn(II))_2$ spectra are distinctly different from uncoupled, mononuclear (Mn(II)) EPR spectra, which consist of a six-line pattern separated by 90 G and typically centered at $g = 2$. The binuclear signal arises from exchange coupling of the two metals through the hydroxide bridge (*11*). The set of 45 G separated hyperfine lines around $g = 2.2$ have previously been assigned to originate from the $S = 2$ spin manifold of an antiferromagnetically coupled $(Mn(II))_2$ system via simulation of the experimental spectra (*11*). The thermal population and depopulation of this spin state can be monitored by the gain and loss of the amplitude of these 45 G split signals near $g = 2.2$. Only a few peaks of the binuclear signal are observed at 3.6 K (e.g., Figures 3−5A). Upon raising the temperature, the multiple 11-line splittings of the Mn/Mn-PTE spectrum are observed with the greatest signal intensity approaching 20 K (*11*). The reduction of this signal above 20 K is observed and results from the depopulation of the spin state from which it arises. The strength of the exchange coupling between the two metals is reflected in the ease of thermal population of spin states

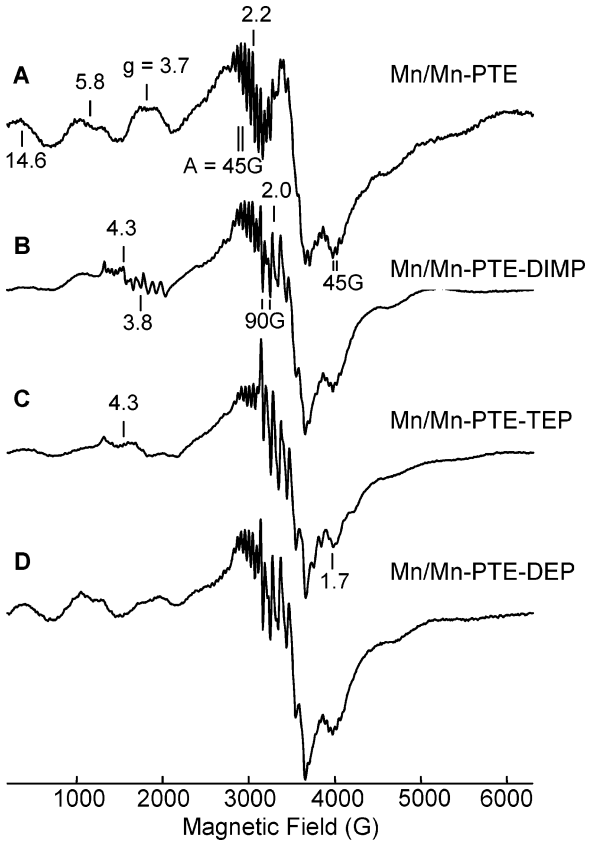

FIGURE 1: EPR spectra of Mn/Mn-PTE upon addition of inhibitors and product. (A) 200 μM Mn/Mn-PTE, 3 scans; (B) 200 μM Mn/Mn-PTE, 171 mM DIMP, 10 scans; (C) 130 μM Mn/Mn-PTE, 350 mM TEP, 20 scans; (D) 115 μM Mn/Mn-PTE, 350 mM DEP, 20 scans. All samples contained 50 mM HEPES buffer, pH 8.0. EPR conditions: temperature, 10 K; microwave power, 2 mW; modulation amplitude, 20 G.

and monitored by the temperature dependence of the signal intensity arising from a given spin state.

Figure 2A is an expansion of the low-field region of Figure 1A. Three broad resonances are observed with *g*-values of 14.6, 5.8, and 3.7. The signal intensities of the broad signals at $g = 14.6$, 5.8, and 3.7 are maximized at lower temperatures and readily observed at 3.6 K. These signals, and other broad signals observed closer to $g = 2$ whose amplitudes increase at lower temperatures, are attributed to $S = 1$ spin states. Signals with 45 G hyperfine splittings are assigned to the binuclear $(Mn(II))_2$ center, whereas signals with 90 G hyperfine splittings arise from uncoupled, monomeric Mn(II).

EPR Spectrum of Mn/Mn-PTE-(DIMP). The addition of DIMP to PTE causes two major changes in the EPR spectrum. The first change is the loss in amplitude of the binuclear signal at $g = 2.2$ and a resulting gain in the mononuclear signal (90 G splittings) at $g = 2.0$ (Figure 1B). The second change is the appearance of two new hyperfine-split signals at $g = 4.3$ and $g = 3.8$ (Figures 1B and 2B). The signal centered at $g = 4.3$ consists of 11 lines separated by 45 G indicative of the spin-coupled binuclear $(Mn(II))_2$ center. The second signal centered at $g = 3.8$ has six lines separated by 90 G reflecting an uncoupled, mononuclear Mn(II) center. These signals indicate that both mononuclear Mn(II) and binuclear centers are present in the DIMP-bound sample.

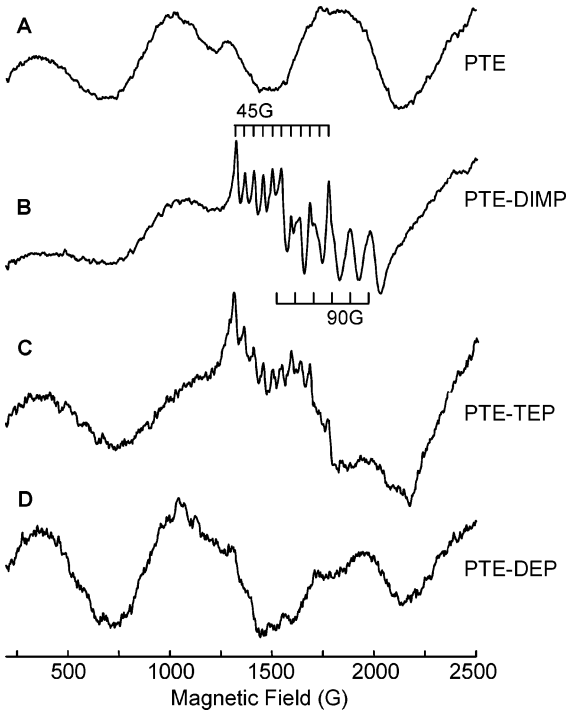

FIGURE 2: Expanded regions of the EPR spectra for Mn/Mn-PTE upon addition of inhibitors and product. (A) 200 μM MnPTE, 30 scans, modulation amplitude 20 G; (B) 200 μM Mn/Mn-PTE, 171 mM DIMP, 20 scans, modulation amplitude 15 G; (C) 130 μM Mn/Mn-PTE, 350 mM TEP, 30 scans, modulation amplitude 15 G; (D) 115 μM Mn/Mn-PTE, 350 mM DEP, 20 scans, modulation amplitude 20 G. All samples contained 50 mM HEPES buffer, pH 8.0. EPR conditions: temperature, 10 K; microwave power, 2 mW.

The EPR spectrum of Mn/Mn-PTE without DIMP (Figure 1A) does not show residual mononuclear Mn(II) signals. DIMP is not expected to chelate Mn(II) ions from the enzyme active site since it lacks chelating functional groups. As described in Materials and Methods, all PTE samples are treated with an ion-exchange column to remove unbound Mn(II) prior to preparation of the EPR samples. Therefore, the mononuclear Mn(II) EPR signals observed upon addition of DIMP are assigned to bound Mn(II) remaining in the active site, and all changes in the spectrum report on interactions of DIMP with the metal center.

The EPR spectrum of PTE with the addition of DIMP reflects more than one active site species in the EPR sample. The decrease in the binuclear signal at $g = 2.2$ and appearance of a mononuclear signal at $g = 2.0$ suggests that binding of DIMP results in the breaking of the hydroxide bridge to one of the metal ions. The loss of the binuclear signal in the EPR spectrum of Mn/Mn-PTE has previously been observed at lower pH and was determined to result from the loss of the hydroxide bridge upon protonation to a water molecule (*11*). The temperature dependence for the remaining binuclear signal at $g = 2.2$ in the Mn/Mn-PTE-(DIMP) sample is nearly identical to that of Mn/Mn-PTE without addition of DIMP (Figure 3, and data not shown). Therefore, the binuclear signal at $g = 2.2$ in Mn/Mn-PTE-(DIMP) reports on a relatively undisturbed binuclear center. Unlike the temperature dependence of the binuclear signal at $g = 2.2$, the new binuclear signal at $g = 4.3$ exhibits a strong signal intensity at the lowest temperature measured of 3.6 K (Figure 3B). A loss in signal intensity is observed above 7 K. The new 45 G split signal at $g = 4.3$ is assigned to the

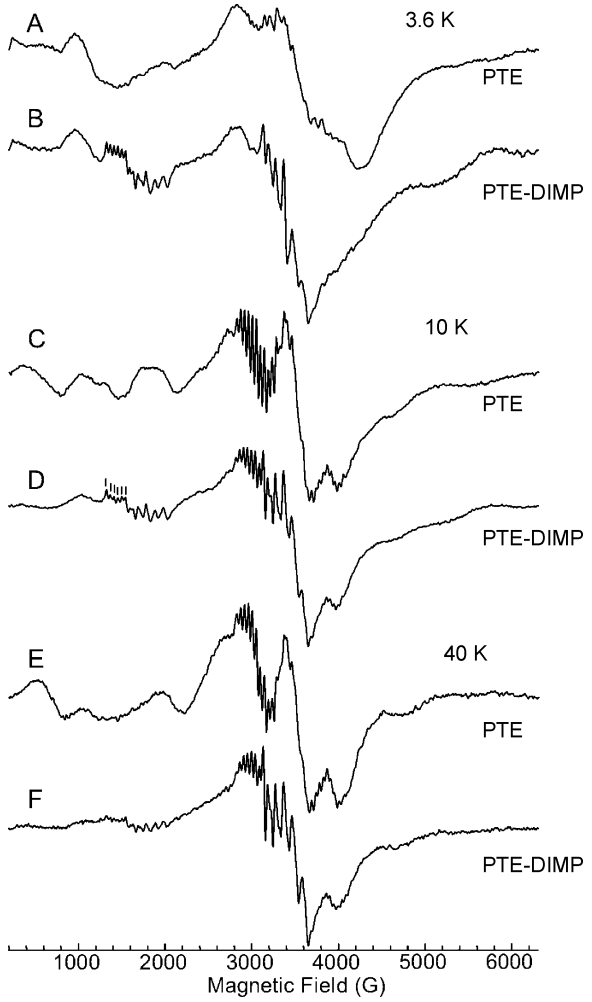

FIGURE 3: EPR spectra of Mn/Mn-PTE with and without the inhibitor DIMP at various temperatures. (A, C, E) 200 μM Mn/Mn-PTE, 10 scans; (B, D, F) 200 μM Mn/Mn-PTE with 171 mM DIMP added, 3 scans; (A, B) 3.6 K; (C, D) 10 K; (E, F) 40 K. Vertical bars designate peaks used to monitor signal intensity at $g = 4.3$ All samples contained 50 mM HEPES buffer, pH 8.0. EPR conditions: microwave power, 2 mW; modulation amplitude, 20 G.

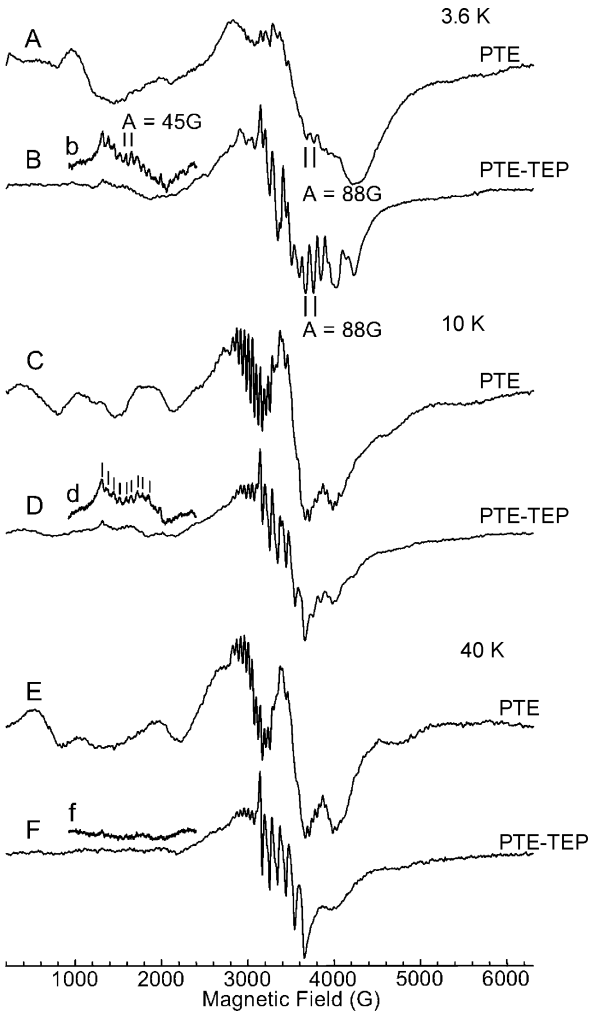

FIGURE 4: EPR spectra of Mn/Mn-PTE with and without the inhibitor TEP at various temperatures. (A, C, E) 200 μM Mn/Mn-PTE, 10 scans; (B, D, F) 130 μM Mn/Mn-PTE with 350 mM TEP added, 5 scans; (A, B) 3.6 K; (C, D) 10 K; (E, F) 40 K. Inset: (b, d, f) Expanded region of 2000−4500 G, 20 scans, vertical bars designate peaks used to determine signal intensity. All samples in 50 mM HEPES buffer, pH 8.0. EPR conditions: microwave power, 2 mW; modulation amplitude, 20 G.

$S = 1$ spin state based on the appearance of this binuclear signal at the lower temperature of 3.6 K and its loss at higher temperatures.

The binuclear and mononuclear Mn(II) EPR signals at $g = 4.3$ and 3.8 are assigned as $\Delta M_s = \pm 2$ forbidden transitions. These half-field or forbidden transitions are observed for Mn(II) species in low-symmetry environments (*13*−*19*). An increase in the zero-field parameter, *D*, reflects the lowering of symmetry at the metal center upon binding of DIMP and results in the observation of these forbidden transitions. The appearance of a mononuclear Mn(II) EPR signal with additional half-field features at $g = 3.8$ does not appear to be due to the loss of the hydroxide bridge alone. An EPR spectrum of untreated Mn/Mn-PTE at pH 6.0 reflects the loss of the hydroxide bridge in the active site, but forbidden half-field transitions are not observed in this spectrum (*11*). Therefore, the appearance of the new low-field mononuclear Mn(II) signal at $g = 3.8$ is due to the presence of DIMP and not just the loss of the hydroxide bridge. The observation of forbidden transitions corresponding to both binuclear and mononuclear centers suggests that DIMP binding occurs at metal centers with and without the hydroxide bridge present. These two active site complexes account for all of the species observed in the EPR spectrum for Mn/Mn-PTE-(DIMP).

EPR Spectrum of Mn/Mn-PTE-(TEP). The inhibitor TEP was added to Mn/Mn-PTE at a final concentration of 350 mM. The addition of TEP to the enzyme results in three major changes in the EPR spectrum (Figures 1C, 2C, and 4). The first is the decrease in the amplitude of the binuclear signal at $g = 2.2$ and gain of a mononuclear Mn(II) signal at $g = 2.0$, which is attributed to the loss of the hydroxide bridge upon addition of TEP. The second change is the appearance of a forbidden transition at $g = 4.3$ consisting of an 11-line splitting separated by 45 G indicative of a spin-coupled $(Mn(II))_2$ center (Figure 2C). Unlike the Mn/Mn-PTE-(DIMP) spectrum, no new half-field feature from a mononuclear Mn(II) signal is observed at $g = 3.8$ for Mn/Mn-PTE-(TEP). The temperature dependence of the binuclear signal at $g = 2.2$ corresponds with the temperature dependence observed for untreated Mn/Mn-PTE, indicating that the exchange coupling in the binuclear center is

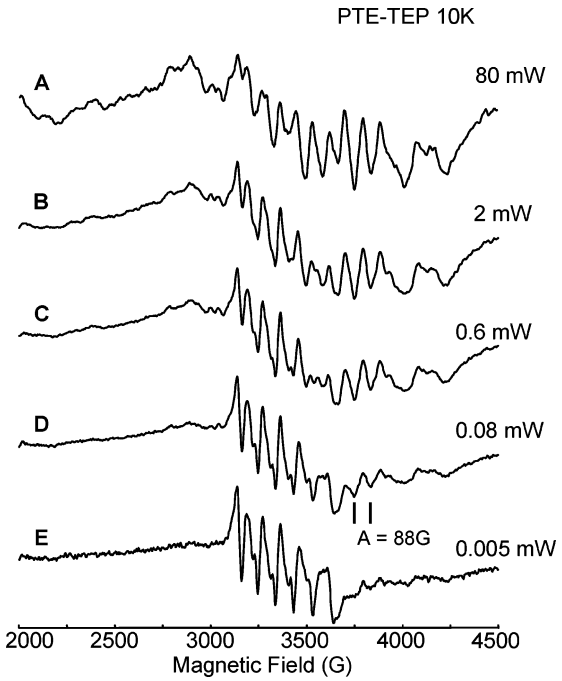

FIGURE 5: EPR spectra of Mn/Mn-PTE-(TEP) sample at various power levels. (A) 80, (B) 2, (C) 0.6, (D) 0.08, and (E) 0.005 mW. 130 μM Mn/Mn-PTE and 350 mM TEP in 50 mM HEPES buffer, pH 8.0. EPR conditions: temperature, 10 K; modulation amplitude, 20 G; 5 scans.

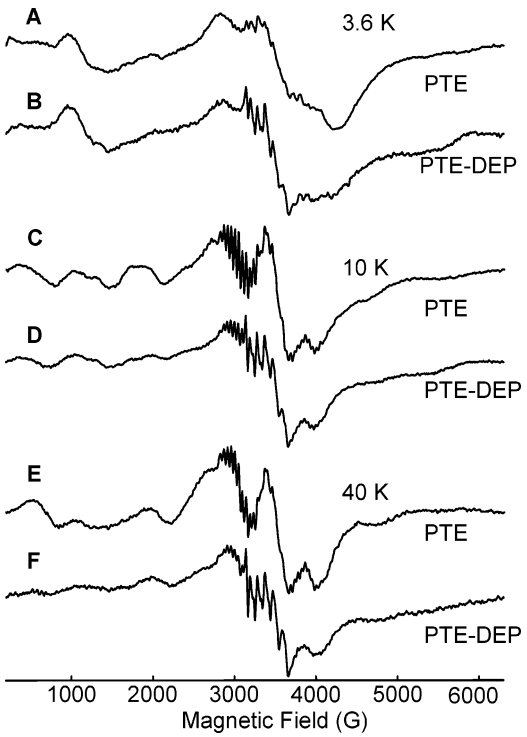

FIGURE 6: EPR spectra of Mn/Mn-PTE with and without the product DEP at various temperatures. (A, C, E) 200 μM Mn/Mn-PTE, 10 scans (B, D, F) 115 μM Mn/Mn-PTE with 350 mM DEP added, 8 scans (A, B) 3.6, (C, D) 10, and (E, F) 40 K. All samples contained 50 mM HEPES buffer, pH 8.0. EPR conditions: microwave power, 2 mW; modulation amplitude, 20 G.

unchanged. As observed for the Mn/Mn-PTE-(DIMP) sample, the binuclear signal at $g = 4.3$ has higher intensity at lower temperatures and is assigned to the $S = 1$ spin state. This signal is assigned to the forbidden transition between the $M_s -1$ and $+1$ levels within the $S = 1$ manifold and reflects binding of TEP to the spin-coupled metal center. The appearance of a forbidden transition upon inhibitor binding results from an increase in the zero-field splitting parameter upon lowered symmetry at the metal center. The binuclear signal at $g = 4.3$ in the Mn/Mn-PTE-(DIMP) spectrum appears stronger than in the Mn/Mn-PTE-(TEP) spectrum (Figure 2B,C) and is due to a greater concentration of binuclear species in the sample, which is also observed by comparing the amount of binuclear signal at $g = 2.2$ in the two samples (Figure 1B,C). The absence of the 90 G split half-field feature for a mononuclear Mn(II) signal at $g = 3.8$ in the Mn/Mn-PTE-(TEP) spectrum suggests a higher symmetry in the uncoupled metal center than observed for the Mn/Mn-PTE-(DIMP) sample. This may result from a weaker coordination of TEP to the mononuclear Mn(II) metal ion due to the distance, orientation, or both about the metal center.

The third change in the EPR spectrum of Mn/Mn-PTE-(TEP) is the appearance of a new signal at $g = 1.7$ with 88 G splittings, observed at temperatures from 3.6 to 15 K (Figure 4B and 5). The temperature dependence of this signal could not be accurately determined due to the presence of the underlying binuclear signal of Mn/Mn-PTE. In an attempt to characterize this new EPR signal, the temperature was held constant at 3.6 K, where there is little population of the signal from the binuclear $(Mn(II))_2$ center of Mn/Mn-PTE. The power at which the spectrum was collected was varied from 5 μW to 80 mW (Figure 5). At 5 μW, the only appreciable signal remaining is the six-line mononuclear Mn(II) signal centered at $g = 2.0$. As the microwave power is increased, the signal in question begins to appear and dominates the spectrum at 80 mW microwave power. The mononuclear Mn(II) signal is still present, however, and so the total number of features assigned to this new signal cannot be determined due to overlap. Two peaks centered at $g = 1.7$ and separated by 88 G are due to the new signal and do not overlap with the standard mononuclear Mn(II) signal. Upon closer inspection of an untreated Mn/Mn-PTE sample at 3.6 K, two peaks separated by 88 G and lying at the same field position as those observed for the new signal were identified (Figure 4A). These two peaks are almost lost in the dominant absorbance of a broad signal from the binuclear $(Mn(II))_2$ center that spans the $g = 1.7$ region. Binding of TEP to the metal center of Mn/Mn-PTE may increase the *D*-strain in the system and broaden the signal from the native species, allowing the 88 G hyperfine splittings at $g = 1.7$ to be observed. The origin of this type of signal is not yet understood, but the 88 G hyperfine splitting suggests that it is due to a distorted mononuclear Mn(II) center.

EPR Spectrum of Mn/Mn-PTE-(DEP). DEP, a product of paraoxon hydrolysis, was added to the enzyme at a final concentration of 350 mM. The EPR spectrum at 10 K reveals a loss of the binuclear signal at $g = 2.2$ and the appearance of a mononuclear Mn(II) signal at $g = 2.0$ (Figures 1D and 6). While this result is also observed upon addition of both DIMP and TEP to the enzyme, the spectrum of enzyme with DEP is unchanged in the low-field region **(**Figure 2D) where the new forbidden transitions at $g = 4.3$ and 3.8 were observed in the presence of the two inhibitors. The loss of binuclear signal and gain in the mononuclear Mn(II) signal is assigned to the loss of the hydroxide bridge. Mn/Mn-PTE-

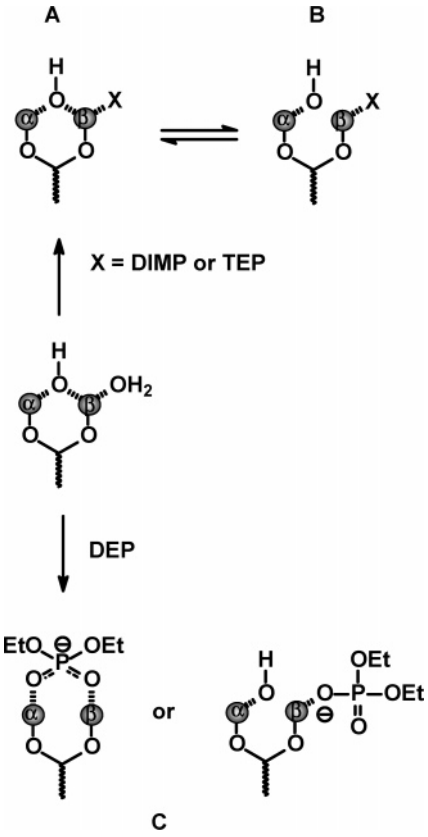

FIGURE 7: Proposed binding of DIMP, TEP, and DEP to the metal center. (Center) The resting state of the enzyme is represented by the active site metals with a terminally bound water ligand and the hydroxide and carboxylate bridges. (A) Terminal water is displaced by DIMP or TEP. (B) Terminal water is displaced by DIMP or TEP with loss of the hydroxide bridge to a terminally bound water or hydroxide. (C) Two possible binding modes: DEP forms a bidentate bridge displacing the hydroxide bridge and the terminally bound water; DEP displaces terminal water with loss of the hydroxide bridge.

(DEP) EPR spectra obtained at different temperatures are shown in Figure 6. Although it is lower in amplitude, the temperature dependence of the binuclear signal in the Mn/Mn-PTE-(DEP) sample is very similar to the dependence exhibited by the same signal from untreated PTE (data not shown). No additional changes are observed in the EPR spectrum of DEP-treated PTE. The absence of forbidden transitions in the Mn/Mn-PTE-(DEP) spectrum suggests that the interaction between the product and the metal center differs from the interaction between the inhibitors and enzyme active site.

DISCUSSION

EPR spectra were obtained in order to investigate the interaction of inhibitors and products with the metal center of Mn/Mn-PTE. The objective of this study was to further an understanding of the mechanism by which organophosphate hydrolysis occurs within the active site of PTE. A schematic representation summarizing the postulated species present within the active site of Mn/Mn-PTE in the presence of inhibitors and product is shown in Figure 7.

Inhibitor Binding at the Metal Center of Mn/Mn-PTE. The EPR spectra for Mn/Mn-PTE-(DIMP) and Mn/Mn-PTE-(TEP) reflect two species in which inhibitor is bound at the metal center. The first species is represented in Figure 7A as inhibitor bound to the metal center with the hydroxide bridge present. In the spectra of inhibited enzymes, an 11-line hyperfine splitting separated by 45 G associated with an exchange-coupled $(Mn(II))_2$ center is observed at $g = 4.3$ as a forbidden transition (Figures 1B/C and 2B/C). No other new species attributable to binuclear $(Mn(II))_2$ centers are observed in these spectra. The appearance of the forbidden transition only in samples treated with inhibitor indicates that a bridged binuclear $(Mn(II))_2$ species is present that experiences an electronic environment that has a lower symmetry in the presence of inhibitor. Similar forbidden transitions have been observed for other Mn(II)-substituted binuclear enzymes, such as bacteriophage λ protein phosphatase and dinitrogenase reductase-activating glycohydrolase, and also in binuclear $(Mn(II))_2$ model complexes (*13*−*15*).

The observed double quantum transition indicates an increase in the zero-field parameter associated with the exchange-coupled $(Mn(II))_2$ center. The increase in zero-field splitting is attributed to the replacement by the inhibitor of a water ligand coordinated to one of the metals. Crystal structures of PTE with DIMP and TEP reveal that the phosphoryl oxygen of the inhibitors displaces a water ligand from the active site (*8*). The larger inhibitor may result in a different orientation of the ligand sphere about the metal center (*3*). This difference may result in a ligand field with lower symmetry and an increase in the zero-field parameter.

It is not possible to distinguish to which metal ion the inhibitors are bound from these EPR spectra alone. Crystal structures of Zn/Zn-PTE with DIMP and TEP bound in the active site reveal the presence of the hydroxide bridge in both cases. The phosphoryl oxygen of DIMP is 2.5 Å from the β-metal, whereas the oxygen of TEP is located 3.4 Å from the metal ion (*8*). Binding of DIMP at the β-metal places the phosphorus center 3.3 Å from and in line with the hydroxide bridge, which would facilitate nucleophilic attack in the case of bound substrate. Binding of substrate to the same β-metal is supported by kinetic studies in which substrate hydrolysis is influenced by polarization of the phosphoryl-oxygen resulting from direct ligation to the metal center (*9*).

The second species present in the Mn/Mn-PTE-(DIMP) and Mn/Mn-PTE-(TEP) samples is represented in Figure 7B as the binding of inhibitor to the metal center with loss of the hydroxide bridge. This species is identified by the diminution of the multiple 11-line hyperfine splittings separated by 45 G at $g = 2.2$ arising from the exchange-coupled $(Mn(II))_2$ center, and gain of signals with six-line hyperfine splittings of 90 G from mononuclear Mn(II) ions at $g = 3.8$ and 2.0. The six-line signal at $g = 3.8$ is observed in the Mn/Mn-PTE-(DIMP) spectrum and arises from a formally unallowed double quantum transition indicating that one or both Mn(II) ions have lowered symmetry. Mononuclear Mn(II) EPR spectra reflecting the loss of the hydroxide bridge in the absence of inhibitor have been observed for Mn/Mn-PTE at low pH and do not exhibit obvious forbidden transitions at lower field (*11*); therefore, the appearance of the signal at $g = 3.8$ in the Mn/Mn-PTE-(DIMP) spectrum is due to inhibitor binding. These data indicate that DIMP bound to the uncoupled metal center increases the zero-field parameter enabling the observation of the double quantum transition. The increase in the zero-field parameter is attributed, as described above, to the

coordination of the phosphonate in place of a water ligand. EPR spectra exhibiting double quantum transitions from a mononuclear Mn(II) ion have been observed for other Mn(II)-containing binuclear metalloenzymes including ribonucleotide reductase, methionine aminopeptidase, and bacteriophage λ phosphoprotein phosphatase (*16*−*18*).

The EPR spectrum for mononuclear Mn(II) in bacteriophage λ phosphoprotein phosphatase (λPP) showed an increase in the $g = 4$ forbidden transition upon a single O/N atom substitution in the ligand field via an asparagine to histidine mutation (*19*). While there is not a crystal structure for this mutant, the effects of this substitution on a binuclear metal center may be inferred from the crystal structures of wild-type arginase and the mutant, H101N (*20*), that showed only minor differences in ligand environments. The EPR spectral effects of the λPP asparagine to histidine mutation demonstrate the ability to detect small changes in the Mn(II) ligand field in these mixed O/N coordination spheres and support the assignment of a change in the ligand field upon displacement of water with DIMP in Mn/Mn-PTE to the observed EPR spectral changes.

The absence of the forbidden transition at $g = 3.8$ for the mononuclear Mn(II) EPR signal distinguishes the binding of TEP as slightly different from that observed for DIMP. This may be due to a weaker coordination of TEP at the metal center. The crystal structures of enzyme with the inhibitor have shown that the phosphoryl oxygen of TEP is located 1 Å further from the β-metal than the phosphoryl oxygen of DIMP (*8*). A weaker coordination would reduce the zero-field parameter so that only allowed transitions are easily observed. Zero-field distortion is, however, evident in the binuclear $(Mn(II))_2$ signal from Mn/Mn-PTE-(TEP), which does exhibit half-field transitions.

A change in the equilibrium constant between the bridged and nonbridged hydroxide species upon inhibitor binding is reflected in the EPR spectra of Mn/Mn-PTE with these two different inhibitors. The observation of both bridged and mononuclear Mn(II) species indicates that the presence of inhibitor shifts the equilibrium such that it no longer favors the bridged species. The replacement of a terminally bound water with a phosphonate analogue could result in an electronic difference that destabilizes the bridged species. The stabilization of the nonbridged species may also result from an adjustment in the metal−metal distance. The shift in equilibrium induced by inhibitor binding suggests that substrate binding at the metal center would induce an analogous shift in equilibrium, resulting in a terminally bound hydroxyl poised for nucleophile attack on the substrate.

The results observed here by EPR spectroscopy predict that the binding of inhibitors DIMP or TEP to the PTE active site results in an equilibrium shift toward a nonbridged species. By contract, the X-ray crystal structures with these inhibitors exhibit only the μ2-hydroxo-bridged species. There are several possible reasons for this descrepancy. One major difference between the two studies is the metal ion: the X-ray structures are of Zn(II)-substituted PTE (*8*), whereas these EPR studies necessarily use Mn(II) PTE. A prior crystallographic study shows that, in comparison with Zn(II), the ligand sphere on the more exposed metal ion in Mn(II)-substituted PTE has expanded to include an additional aqua ligand (*5*). This is consistent with the slightly larger ionic radius of Mn(II), which may similarly allow for a closer approach of the potential phosphonate oxygen ligand from DIMP or TEP than is observed crystallographically for the Zn(II)-substituted enzyme, thereby producing a higher yield of the unbridged species. It is also possible that the crystallographic study reveals only one of the possible conformations. At least two prior studies (*26*, *27*) have reported separate bridging conformations in different crystal forms of binuclear $(Mn(II))_2$ sites in proteins, wherein one form includes a single-atom bridging molecule from solvent and the other retains only μ-1,3-bridged carboxylate ligands, much longer Mn−Mn distances, and presumably much weaker spin-exchange interactions. In both of these cases, the different bridging scenarios are accompanied by very slight changes in protein conformation. EPR studies are performed on solutions that have been frozen over a ~1 s time interval, and they may capture a different population distribution than that selected in crystallized samples.

Influence of Product on the Metal Center of Mn/Mn-PTE. The presence of DEP at the metal center is indicated by the decrease in amplitude of the binuclear signal and gain in a mononuclear Mn(II) signal around $g = 2$. The decrease in the exchange-coupled $(Mn(II))_2$ signal reflects loss of the hydroxide bridge. The absence of observed forbidden transitions suggests that the change in the zero-field parameter or ligand field is negligible in comparison with the change in the ligand field induced by binding of DIMP or TEP. For the dimanganese center of λPP, coordination by inorganic phosphate resulted in a shift in temperature dependence of the binuclear $(Mn(II))_2$ EPR signal due to an apparent decrease in the strength of the exchange coupling (*19*). The overall EPR spectrum for λPP was less affected by the addition of phosphate, however, than by single point mutations for residues coordinated to the metal core (*18*) or by binding of other oxoanions (*19*). The Mn/Mn-PTE-(DEP) and λPP-(phosphate) spectra reveal the disruption of the solvent bridge by a phosphate and a less pronounced effect on the ligand field than observed with other coordinating ligands. Potential binding of DEP as either monodentate or bidentate ligation to the metal center without the hydroxyl bridge is presented in Figure 7C.

Support for the bidentate coordination of DEP is found in the crystal structure of PTE from *Agrobacterium radiobacter* in which hydrolysis of substrate resulted in bidentate coordination of the product, dimethyl thiophosphate, at the metal center (*21*). Binding of this product revealed the phosphoryl sulfur bound 2.5 Å from the β-metal, which is also consistent with the phosphoryl oxygen position of DIMP with respect to the β-metal. Crystal structures of other binuclear enzymes with phosphate and sulfate bound at the active site also support the binding modes represented in Figure 7C. Bidentate coordination of phosphate has been observed for purple acid phosphatase (*22*, *23*). Crystal structures of purple acid phosphatase and λPP with sulfate bound exhibit both terminal and bridged coordination to the metal center (*24*, *25*).

The crystal structures of PTE with DIMP, TEP, and product all show coordination modes in which the hydroxide bridge is still present. By contrast, the EPR data presented in this work support a shift in equilibrium toward comparable amounts of bridge and nonbridged hydroxide species upon binding of DIMP or TEP and do not exclude the same shift in equilibrium upon product binding. Therefore, in solution,

both bridged and nonbridged hydroxide species may be present with product bound.

This work concludes that binding of inhibitor to the binuclear active site of PTE occurs at the metal center and results in an increase of nonbridged hydroxide species. These results, in conjunction with kinetic and crystallographic data, suggest that substrate binding via the phosphoryl oxygen at the β-metal weakens the hydroxyl bridge coordination to the β-metal. This loss of coordination would increase the nucleophilic character of the bridge and result in a stronger nucleophile for hydrolysis.

REFERENCES

1. Dumas, D. P., Caldwell, S. R., Wild, J. R., and Raushel, F. M. (1989) Purification and properties of the phosphotriesterase from *Pseudomonas diminuta*, *J. Biol. Chem. 264*, 19659−19665.
2. Hong, S. B., and Raushel, F. M. (1997) Inhibitors directed towards the binuclear metal center of phosphotriesterase, *J. Enzyme Inhib. 12*, 191−203.
3. Vanhooke, J. L., Benning, M. M., Raushel, F. M., and Holden, H. M. (1996) Three-dimensional structure of the zinc-containing phosphotriesterase with the bound substrate analog diethyl 4-methylbenzylphosphonate, *Biochemistry 35*, 6020−6025.
4. Benning, M. M., Kuo, J. M., Raushel, F. M., and Holden, H. M. (1994) Three-dimensional structure of phosphotriesterase: an enzyme capable of detoxifying organophosphate nerve agents, *Biochemistry 33*, 15001−15007.
5. Benning, M. M., Shim, H., Raushel, F. M., and Holden, H. M. (2001) High resolution X-ray structures of different metal-substituted forms of phosphotriesterase from *Pseudomonas diminuta*, *Biochemistry 40*, 2712−2722.
6. Omburo, G. A., Kuo, J. M., Mullins, L. S., and Raushel, F. M. (1992) Characterization of the zinc binding site of bacterial phosphotriesterase, *J. Biol. Chem. 267*, 13278−13283.
7. Shim, H., and Raushel, F. M. (2000) Self-assembly of the binuclear metal center of phosphotriesterase, *Biochemistry 39*, 7357−7364.
8. Benning, M. M., Hong, S. B., Raushel, F. M., and Holden, H. M. (2000) The binding of substrate analogs to phosphotriesterase, *J. Biol. Chem. 275*, 30556−30560.
9. Aubert, S. D., Li, Y., and Raushel, F. M. (2004) Mechanism for the hydrolysis of organophosphates by the bacterial phosphotriesterase, *Biochemistry 43*, 5707−5715.
10. Lewis, V. E., Donarski, W. J., Wild, J. R., and Raushel, F. M. (1988) Mechanism and stereochemical course at phosphorus of the reaction catalyzed by a bacterial phosphotriesterase, *Biochemistry 27*, 1591−1597.
11. Samples, C. R., Howard, T., Raushel, F. M., and DeRose, V. J. (2005) Protonation of the binuclear metal center within the active site of phosphotriesterase, *Biochemistry 44*, 11005−11013.
12. Thoden, J. B., Phillips, G. N., Jr., Neal, T. M., Raushel, F. M., and Holden, H. M. (2001) Molecular structure of dihydroorotase: a paradigm for catalysis through the use of a binuclear metal center, *Biochemistry 40*, 6989−6997.
13. Antharavally, B. S., Poyner, R. R., and Ludden, P. W. (1998) EPR spectral evidence for a binuclear Mn(II) center in dinitrogenase reductase-activating glycohydrolase from *Rhodospirillum rubrum*, *J. Am. Chem. Soc. 120*, 8897−8898.
14. Rusnak, F., Yu, L., Todorovic, S., and Mertz, P. (1999) Interaction of bacteriophage lambda protein phosphatase with Mn(II): evidence for the formation of a $[Mn(II)]_2$ cluster, *Biochemistry 38*, 6943−6952.
15. Golombek, A. P., and Hendrich, M. P. (2003) Quantitative analysis of dinuclear manganese(II) EPR spectra, *J. Magn. Reson. 165*, 33−48.
16. Pierce, B. S., and Hendrich, M. P. (2005) Local and global effects of metal binding within the small subunit of ribonucleotide reductase, *J. Am. Chem. Soc. 127*, 3613−3623.
17. Copik, A. J., Nocek, B. P., Swierczek, S. I., Ruebush, S., Jang, S. B., Meng, L., D'Souza, V. M., Peters, J. W., Bennett, B., and Holz, R. C. (2005) EPR and X-ray crystallographic characterization of the product-bound form of the Mn(II)-loaded methionyl aminopeptidase from *Pyrococcus furiosus*, *Biochemistry 44*, 121−129.
18. White, D. J., Reiter, N. J., Sikkink, R. A., Yu, L., and Rusnak, F. (2001) Identification of the high affinity Mn^{2+} binding site of bacteriophage lambda phosphoprotein phosphatase: effects of metal ligand mutations on electron paramagnetic resonance spectra and phosphatase activities, *Biochemistry 40*, 8918−8929.
19. Reiter, N. J., White, D. J., and Rusnak, F. (2002) Inhibition of bacteriophage lambda protein phosphatase by organic and oxoanion inhibitors, *Biochemistry 41*, 1051−1059.
20. Cama, E., Emig, F. A., Ash, D. E., and Christianson, D. W. (2003) Structural and functional importance of first-shell metal ligands in the binuclear manganese cluster of arginase I, *Biochemistry 42*, 7748−7758.
21. Jackson, C., Kim, H. K., Carr, P. D., Liu, J. W., and Ollis, D. L. (2005) The structure of an enzyme-product complex reveals the critical role of a terminal hydroxide nucleophile in the bacterial phosphotriesterase mechanism, *Biochim. Biophys. Acta 1752*, 56−64.
22. Klabunde, T., Strater, N., Frohlich, R., Witzel, H., and Krebs, B. (1996) Mechanism of Fe(III)-Zn(II) purple acid phosphatase based on crystal structures, *J. Mol. Biol. 259*, 737−748.
23. Guddat, L. W., McAlpine, A. S., Hume, D., Hamilton, S., de Jersey, J., and Martin, J. L. (1999) Crystal structure of mammalian purple acid phosphatase, *Struct. Fold. Des. 7*, 757−767.
24. Voegtli, W. C., White, D. J., Reiter, N. J., Rusnak, F., and Rosenzweig, A. C. (2000) Structure of the bacteriophage lambda Ser/Thr protein phosphatase with sulfate ion bound in two coordination modes, *Biochemistry 39*, 15365−15374.
25. Lindqvist, Y., Johansson, E., Kaija, H., Vihko, P., and Schneider, G. (1999) Three-dimensional structure of a mammalian purple acid phosphatase at 2.2 Å resolution with a μ-hydroxo bridged di-iron center, *J. Mol. Biol. 291*, 135−147.
26. Kliegman, J. I., Griner, S. L., Helmann, J. D., Brennan, R. G., Glasfeld, A. (2006) Structural basis for the metal-selective activation of the manganese transport regulator of *Bacillus subtilis*, *Biochemistry 45*, 3493−3505.
27. DeGrado, W. F., Di Costanzo, L., Geremia, S., Lombardi, A., Pavone, V., Randaccio, L. (2003) Sliding helix and change of coordination geometry in a model Di-Mn-II protein, *Angew. Chem., Int. Ed. 42*, 417−420.

BI061951D